

# Linear gyrokinetic simulations of microinstabilities within the pedestal region of H-mode NSTX discharges in a highly shaped geometry

M. Coury,<sup>1,a)</sup> W. Guttenfelder,<sup>1</sup> D. R. Mikkelsen,<sup>1</sup> J. M. Canik,<sup>2</sup> G. P. Canal,<sup>3</sup> A. Diallo,<sup>1</sup> S. Kaye,<sup>1</sup> G. J. Kramer,<sup>1</sup> R. Maingi,<sup>1</sup> and NSTX-U team<sup>1</sup>

<sup>1</sup>Princeton Plasma Physics Laboratory, Princeton University, Princeton, New Jersey 08543, USA

<sup>2</sup>Oak Ridge National Laboratory, Oak Ridge, Tennessee 37831, USA

<sup>3</sup>General Atomics, San Diego, California 92186, USA

(Received 27 April 2016; accepted 15 June 2016; published online 30 June 2016)

Linear (local) gyrokinetic predictions of edge microinstabilities in highly shaped, lithiated and non-lithiated NSTX discharges are reported using the gyrokinetic code GS2. Microtearing modes dominate the non-lithiated pedestal top. The stabilization of these modes at the lithiated pedestal top enables the electron temperature pedestal to extend further inwards, as observed experimentally. Kinetic ballooning modes are found to be unstable mainly at the mid-pedestal of both types of discharges, with unstable trapped electron modes nearer the separatrix region. At electron wavelengths, electron temperature gradient (ETG) modes are found to be unstable from mid-pedestal outwards for  $\eta_{e, \text{exp}} \sim 2.2$ , with higher growth rates for the lithiated discharge. Near the separatrix, the critical temperature gradient for driving ETG modes is reduced in the presence of lithium, reflecting the reduction of the lithiated density gradients observed experimentally. A preliminary linear study in the edge of non-lithiated discharges shows that the equilibrium shaping alters the electrostatic modes stability, which was found more unstable at high plasma shaping. *Published by AIP Publishing.*

[<http://dx.doi.org/10.1063/1.4954911>]

## I. INTRODUCTION

Understanding the complex dynamics of the pedestal region is crucial to achieve optimum energy production in fusion power plants as modeling predicts a fusion gain scaling roughly with the square of the pedestal pressure.<sup>1</sup> However, steep plasma pressure gradients at the edge drive instabilities called Edge Localized Modes (ELMs).<sup>2–8</sup> ELMs produce periodic bursts of energy and particles fluxes onto the plasma-facing component (PFC) of the reactor vessel, causing erosion of the material. Impurities generated by erosion or deuterium recycling from the wall degrade the plasma performance.<sup>9</sup> Lithium-coated walls are proven to both reduce recycling and improve the energy confinement time  $\tau_E$ .<sup>10,11</sup> It is also experimentally observed that ELMs are altered, even suppressed with increasing lithium doses subsequent to the widening of the pedestal region.<sup>12,13</sup> In addition, the plasma shaping is known to affect the plasma performance,<sup>14</sup> with gyrokinetic simulations assessing the shaping effect on core turbulence.<sup>15</sup> The comparative linear gyrokinetic analysis of Ref. 16, performed in an “intermediate” triangularity ( $\delta \sim 0.46$ ), low elongation ( $\kappa \sim 1.8$ ) confinement regime, investigated the effect of lithium coating on the pedestal structure. It was found that at the top of the pedestal region without lithium coating, microtearing (MT) modes<sup>17,18</sup> are dominant, replaced by trapped electron (TE) modes<sup>19–21</sup> with lithium-coated PFCs. Towards the separatrix, electron temperature gradient (ETG) modes<sup>22</sup> were identified as being a limiting factor to the electron temperature  $T_e$  gradient with and without lithium coating. Further, kinetic ballooning (KB) modes,<sup>23–25</sup> candidates for limiting the total pedestal

pressure, were observed for both cases at mid-pedestal. It was also concluded in Ref. 16 that the decrease in the pedestal top energy transport and the widening of the pedestal region in lithiated discharges were related to the stabilization of MT modes by density gradients. The suppression of ELMs in lithiated discharges may be explained by the stiffness of the electron temperature profile due to unstable ETG modes coupled with the strong reduction in the electron density, when compared to a non-lithiated discharge.

Presented herein is a (local) linear gyrokinetic study of pedestal microinstabilities using the gyrokinetic code GS2.<sup>26</sup> This study is based on the experimental data obtained on the National Spherical Torus Experiment (NSTX).<sup>11</sup> The data were obtained from a highly shaped ( $\delta \sim 0.6 - 0.7$ ,  $\kappa \sim 2.2$ ) reference case without lithium coating for comparison to a highly shaped high-dose lithium-coated PFC case. GS2 was successfully used to study, for example, the plasma edge microstability<sup>16,27</sup> and electron-scale instabilities (i.e., high- $k_{\perp}$ , with  $k_{\perp}$  the perpendicular wavenumber), e.g., electron temperature gradient driven turbulence.<sup>28–30</sup> Gyrokinetic codes such as GTC or GYRO were also successfully applied to simulate microinstabilities in the edge of tokamak plasmas.<sup>7,31,32</sup> The validity of the gyrokinetic ordering ( $\rho/L < 1$ ) at the plasma edge, where the profile scale lengths ( $L$ ) may be close to the ion gyroradius ( $\rho_i$ ), was further assessed for the values used in this numerical study. Table I shows the ratios ( $\rho_i/L_{\text{ptot}}$ ) calculated from the experimental results, with  $\rho_i$  the ion gyroradius and  $L_{\text{ptot}}$  the total pressure gradient scale length. The ratios at the pedestal region are  $< 1$ , as imposed by the gyrokinetic ordering. Table I also shows that  $\lambda_{De}/\rho_e < 1$  for the same flux surfaces, eliminating any Debye shielding stabilization of ETG modes in case the electron Debye length

<sup>a)</sup>Electronic mail: mcoury@pppl.gov

TABLE I. Validation of the modeling assumptions for a reference (non-lithiated) discharge #132543 and a lithiated discharge #132588 over a wide range of  $\psi_N$ .

Shot #132543	$\psi_N$	$\lambda_{De}/\rho_e$	$\rho_i/L_{ptot}$
	0.80	0.168	0.033
	0.85	0.174	0.024
	0.90	0.181	0.045
	0.95	0.186	0.139
	0.99	0.238	0.212
Shot #132588	$\psi_N$	$\lambda_{De}/\rho_e$	$\rho_i/L_{ptot}$
	0.75	0.214	0.088
	0.80	0.241	0.119
	0.85	0.268	0.150
	0.90	0.313	0.168
	0.95	0.346	0.160
	0.99	0.380	0.152

( $\lambda_{De}$ ) exceeds the electron gyroradius ( $\rho_e$ ). In addition, a few linear runs including the Debye shielding effect in the Poisson equation were conducted at selected poloidal wavenumbers  $k_\theta$  and  $\Psi_N$ . No clear effect of the Debye shielding parameter on the simulation outputs was observed when compared to similar numerical runs omitting this parameter. Finally, global effects are likely to affect the turbulent transport at the plasma edge, as highlighted in Ref. 33.

The difference between the study reported herein and the work of Ref. 16 is the change in the plasma shaping and the lithium dose that altered the pedestal structure. Here also, the suppression of ELMs and the flattening of the edge density profiles are observed from the lithiated experimental data. The onset of KBM at steep pressure gradients and the reduction of lithiated critical temperature gradients for driving ETG modes are studied. A comparison with the findings of Ref. 16 is discussed, to evaluate the influence of the shaping of flux surfaces on pedestal microinstabilities.

## II. SUMMARY OF EXPERIMENTAL OBSERVATIONS

This numerical analysis is based on a reference (non-lithiated) discharge #132543 and a lithiated discharge #132588 (550 mg pre-discharge lithium deposition). Details of the discharges and extensive discussions on the observations are presented in Ref. 11. The plasma equilibrium parameters are given in the Appendix. Reported in this section are the main findings of Ref. 11 as well as temperature and density profiles that are input parameters in this work. The profile fits in Figure 1 and kinetic numerical equilibria are generated based on experiments, as described in Refs. 11–13 and 16. Figure 1 shows the density  $n_s$ , temperature  $T_s$ , and total pressure  $P_{tot}$  profile fits from  $\Psi_N = 0.6$  to  $\Psi_N = 1.0$  ( $\Psi_N$  is the normalized poloidal flux) for discharge #132543 in black and discharge #132588 in red. Note that the steady neutral beam heating power was 6 MW for the reference shot and 4 MW for the lithiated discharge. Comparing the electron profiles for the two discharges, a widening of the pedestal region is clearly seen for the lithiated discharge. Taking the temperature profile as a reference, the pedestal top (delimited by the arrows in Figure 1(b)) is pushed towards

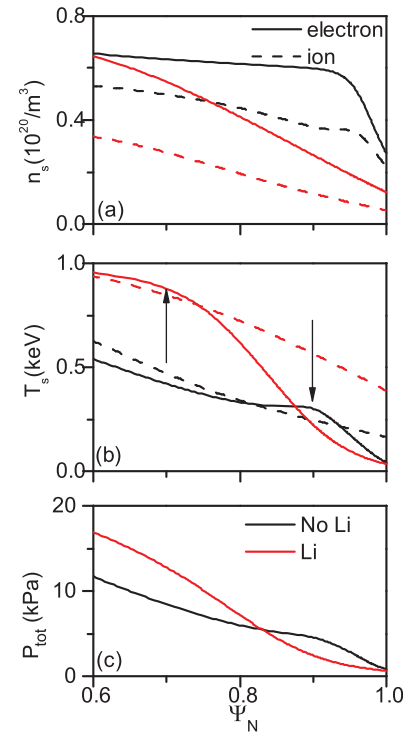


FIG. 1. (a) Species density ( $n_s$ ), (b) temperature ( $T_s$ ), and (c) total pressure ( $P_{tot}$ ) experimentally inferred profiles as a function of  $\psi_N$ . The electron profiles are represented in solid lines, the ion profiles in dashed lines. Profiles of the lithiated discharge are in red, the non-lithiated discharge in black.

the core at around  $\Psi_N \sim 0.7$ , while for the non-lithiated discharge the pedestal top is localized at around  $\Psi_N \sim 0.9$ . Focusing on profiles at  $\Psi_N > 0.9$ , a reduction of the densities is observed for the lithiated discharge. Higher ion temperatures are recorded across the entire minor radius (a) for the lithiated discharge and similar trends are found for the electron temperature profiles, with slightly higher electron temperatures for the reference discharge near the separatrix. The electron density profiles for both discharges merge at around  $\Psi_N \sim 0.6$ , while the ion profiles follow similar trends with lower main ion densities for the lithiated discharge. The non-lithiated electron temperatures are lower by  $\sim 50\%$  at around  $\Psi_N < 0.7$ .

The pressure profiles are also modified with lithiation, as shown in Figure 1(c). For instance, the flattening of the lithiated density profiles at the edge leads to reduced pressure gradient, which is expected to stabilize peeling-ballooning modes responsible for type-I ELMs. Suppression of ELMs is experimentally observed for the lithiated study case.<sup>11</sup> The reduction in the  $D_\alpha$  emission due to reduced recycling from the wall and an improved energy confinement are also observed. Furthermore, a better deposition scheme of lithium near the outer strike point is obtained in highly shaped discharges<sup>11</sup> when compared to discharges at intermediate shaping.<sup>16</sup> To characterize the plasma edge dynamics with and without lithium evaporation in highly shaped plasmas, the following Secs. III A and III B present results of a linear microinstability study carried out at specific values of  $\Psi_N$  of interest within the pedestal region identified experimentally.

### III. SURVEY OF MODES WITHIN THE PEDESTAL REGION OF HIGHLY SHAPED DISCHARGE

Based on experimental parameters (shots #132543 and #132588), the linear microinstability calculations presented herein are performed using the local gyrokinetic code GS2. The plasma parameters and geometry coefficients are derived from realistic (experimental) gradients and kinetic numerical equilibria. The simulations are fully electromagnetic ( $\phi$ ,  $\delta A_{\parallel}$ ,  $\delta B_{\parallel}$ ), including a pitch angle scattering collision operator and three plasma species deuterium  $D$ , carbon  $C$ , and electrons  $e$ . In all calculations, the ballooning parameter  $\theta_0$ <sup>34</sup> is set to zero, the usual location of the maximum growth rates.<sup>35</sup> A few scans over the ballooning parameter were performed with no major increase in the growth rate values when compared to the values at  $\theta_0 = 0$ . To insure sufficient numerical resolution, convergence tests (e.g., GS2 grid convergence tests including the extent of the poloidal angle  $\theta$  or the time step  $\delta t$ ) were performed. Numerical tests were also carried out to reproduce published trends, e.g., the CYCLONE base case<sup>36</sup> and some linear edge simulations of Ref. 16. The convergence was assessed by comparing the resulting growth rates ( $\gamma$ ), real frequencies ( $\omega$ ), and eigenfunction structures.

Figure 2 presents example spectra of real frequencies and growth rates of the most unstable eigenmode as a function of wavenumber  $k_{\theta}\rho_s$  with  $\rho_s$  the ion gyroradius at electron temperature, for the reference #132543 (a)–(d) and the lithiated #132588 (e)–(h) discharges. For both discharges, the calculations are performed at the pedestal top, the mid-pedestal (around the steepest gradients), and near the separatrix as defined in the temperature profiles of Figure 1(b). Before getting into a detailed mode analysis, a first observation is that real frequency spectra at low- $k_{\theta}$  are mainly formed by groups or “branches of modes,” e.g., the branch enclosed by the green rectangle in Figure 2(a). These branches are a consequence of competing eigenmodes to be identified by their eigenfunctions and series of parameter scans as described below. In addition, taking as an example the spectra of Figure 2(e), when moving from  $\psi_N = 0.90$  to  $\psi_N = 0.99$  the nature of the most unstable modes changes from modes strictly propagating in the ion diamagnetic direction ( $\omega > 0$  in GS2) to a combination of modes propagating in both the electron and ion diamagnetic directions. In contrast, spectra at high- $k_{\theta}$  show single branches with “continuous” trends mainly with modes having negative real frequency corresponding to the electron diamagnetic direction modes (e.g., ETG). The spectrum at  $\psi_N = 0.70$  for the lithiated  $T_e$  profile pedestal top is not shown in Figure 2 because most  $k_{\theta}\rho_s$  are stable; a few tearing parity modes are found unstable at high- $k_{\theta}$ , as discussed in Section III A. The ion-scale and electron-scale wavenumbers are discussed in separate sections for clarity. In this survey, the modes are identified by the parity of the eigenfunctions and the sign of the real frequencies associated with wavenumbers of interest, as summarized in Table II. These wavenumbers are parts of branches appearing in the spectra. To strengthen the mode identification, parameter scans around the experimental values are performed without varying the original

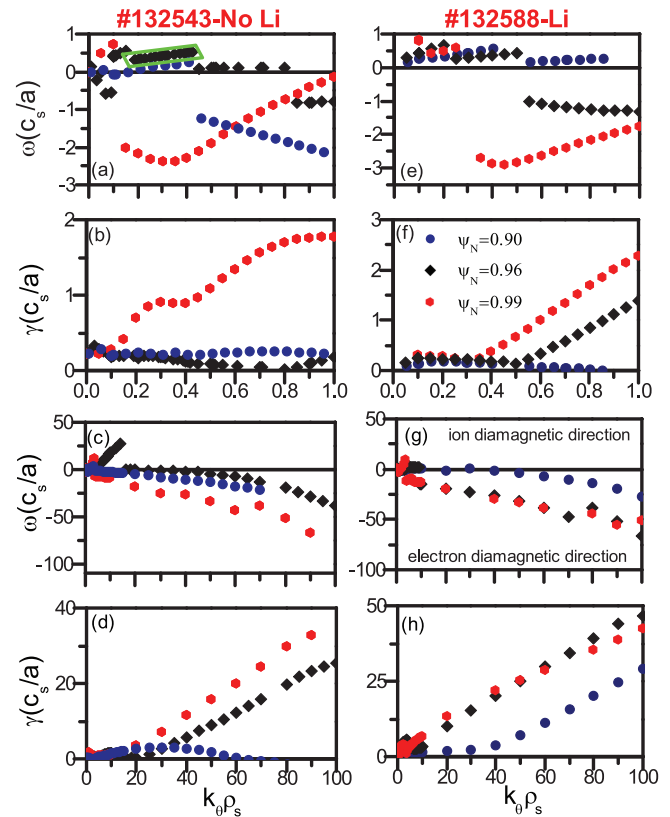


FIG. 2. Spectra of real frequencies ( $\omega$ ) and growth rates ( $\gamma$ ) of the fastest growing eigenmodes at  $\psi_N = 0.90, 0.96, 0.99$  for the reference discharge #132543 (a)–(d) and the lithiated discharge #132588 (e)–(h). The eigenvalues (both in units of  $c_s/a$ , with  $c_s = \sqrt{T_e/m_i}$  the sound speed,  $T_e$  and  $m_i$  are the electron temperature and ion mass, respectively) of the fastest growing eigenmodes are plotted as a function of wavenumbers  $k_{\theta}\rho_s$ . (a), (b), (e), and (f) show scans for  $k_{\theta}\rho_s \leq 1$ , i.e., the ion-scale wavenumbers and (c), (d), (g), and (h) show scans for  $0 < k_{\theta}\rho_s \leq 100$ , i.e., the electron-scale wavenumbers.

geometry parameters. For example, scans over the electron  $\beta \propto n_e T_e / B_T^2$  ( $B_T$  is the toroidal magnetic field) parameter may also be required to characterize pedestal instabilities for the NSTX high- $\beta$  plasmas.<sup>37</sup> The extensive work of Ref. 18 on MT modes in NSTX plasmas shows that microtearing modes, producing electron thermal transport, are driven by electron temperature gradients above critical  $\beta$  values. MT modes are stabilized by increasing normalized density gradients. Finally on the long-scale wavelength, TEM modes are driven by electron density and temperature gradients. TEM modes are a source of both particle and heat transport. On a short-scale wavelength, scans around the experimental normalized electron temperature gradient scale length  $a/L_{T_e}$  are performed to find the critical temperature gradient for ETG modes.<sup>29</sup>

#### A. Ion-scale wavenumbers

Table III summarizes the main low- $k$  instabilities ( $0.1 \leq k_{\theta}\rho_s \leq 1$ ) identified for both discharges in the  $T_e$  pedestal region, as discussed below. At first, the modes identified at the pedestal-top of both discharges are presented, followed by the modes identified at mid-pedestal and near the separatrix. A parameter scan performed at mid-pedestal

TABLE II. Summary of linear instabilities.  $Q_e$  and  $S_e$  are electron heat and particle fluxes, respectively. es and em stand for electrostatic and electromagnetic.  $C_{ei}$  stands for electron-ion collisions.

	Electromagnetic		Electrostatic		
	KBM	MTM	TEM	ETG	ITG
Driven by	$\omega > 0$ , low- $k$ $\beta$ , $(a/L_T, n)$	$\omega < 0$ , low- $k$ $\beta$ , $a/L_{T_e}$ ( $\eta_e$ )	$\omega < 0$ , intermediate- $k$ $a/L_{T_e}$ , $a/L_n$	$\omega < 0$ , high- $k$ $a/L_{T_e}$ ( $\eta_e$ )	$\omega > 0$ , low- $k$ $a/L_{T_i}$
Stabilized by	$\beta < \beta_{crit}$	$\beta < \beta_{crit}$ , high $a/L_n$	$C_{ei}$	$a/L_n$	$a/L_n$ , $\beta$ , $\gamma_{E \times B}$
Parity	Ballooning parity	Tearing parity			
Fluxes		$Q_e^{em}$	$Q_e^{es} - S_e^{es}$	$Q_e^{es}$	$Q_i^{es}$

TABLE III. Identification of low- $k$  linear instabilities.

	High shaping	
	No lithium	Lithium
$\Psi_N = 0.7$		MTM ( $k_\theta \rho_s = 4 - 5.5$ )
$\Psi_N = 0.9$	MTM ( $k_\theta \rho_s = 0.8$ )	Tearing-parity ( $k_\theta \rho_s = 0.1 - 0.3$ ) $\rightarrow$ KBM ( $k_\theta \rho_s = 0.8$ )
$\Psi_N = 0.96$	Tearing-parity ( $k_\theta \rho_s = 0.3$ ) $\rightarrow$ KBM ( $k_\theta \rho_s = 0.8$ )	
$\Psi_N = 0.99$	TEM ( $k_\theta \rho_s = 0.8$ )	TEM ( $k_\theta \rho_s = 0.8$ )

is shown as an example of analysis supporting the mode identification. Examples of eigenfunction structures are also presented as part of the mode identification.

At the pedestal-top of the *reference discharge* ( $\Psi_N = 0.90$ ), while the growth rate is almost constant across the wavenumber scan, the sign of the real frequency goes from positive to negative with increasing wavenumber values. The modes propagating in the electron diamagnetic direction, identified as MT modes, present tearing parities as shown in the example of Figure 3 (odd  $\phi$  and even  $\delta A_{||}$  around  $\theta = 0$ ). The parameter scans over  $a/L_{T_e}$ ,  $a/L_{T_i}$ ,  $a/L_n$ , and  $\beta$  performed at a wavenumber  $k_\theta \rho_s = 0.8$  show that the MT mode

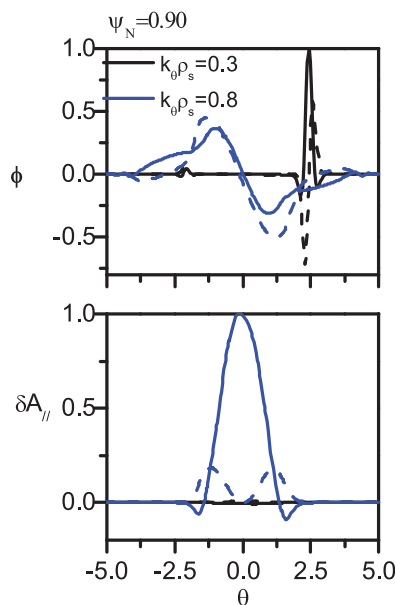


FIG. 3. Normalized field eigenfunctions at  $\Psi_N = 0.90$  (non-lithiated discharge) plotted as a function of the poloidal angle  $\theta$  for  $k_\theta \rho_s$  specified in the legend. In all figures, real and imaginary parts are represented in solid and dashed lines, respectively.

is driven by  $a/L_{T_e} \ll a/L_{T_e, exp}$ . The growth rate of this mode decreases with increasing  $a/L_{T_e} \sim a/L_{T_e, exp}$ ,  $\beta \sim \beta_{exp}$ , and  $a/L_n$  (exp denotes experimental). As for the group of modes propagating in the ion diamagnetic direction, the parameter scan performed at  $k_\theta \rho_s = 0.3$  shows that this mode is relatively insensitive to all the parameters and is suppressed when the gradients are set to zero. Furthermore, the structures of both  $\phi$  and  $\delta A_{||}$  also shown in Figure 3 are difficult to characterize. The amplitude of  $\delta A_{||}$  being much smaller than  $\phi$  suggests that the mode is mainly electrostatic, with  $\phi$  peaking away from  $\theta = 0$  as observed in Refs. 32 and 8 for TEM instabilities at intermediate  $k_\theta \rho_s$ .

Only a few wavenumbers,  $4 < k_\theta \rho_s \leq 5.5$ , are found unstable at the pedestal-top of the *lithiated discharge* ( $\Psi_N = 0.70$ ). The modes are identified as MT modes. The parameter scans performed at  $k_\theta \rho_s = 4.5$  show that the MT mode<sup>18</sup> is driven by  $a/L_{T_e}$  above a critical  $\beta \sim 0.035 < \beta_{exp} \sim 0.1$ .

At the mid-pedestal of the *reference discharge* ( $\Psi_N = 0.96$ ), tearing-parity modes are found unstable for  $0.2 \leq k_\theta \rho_s \leq 0.4$  replaced by unstable ballooning-like eigenmodes (KBM<sup>24,25</sup>) for  $0.4 < k_\theta \rho_s \leq 0.8$ . Figure 4 shows the eigenfunctions associated with the eigenmodes at  $k_\theta \rho_s = 0.3$  and  $0.8$ . As can be seen, both modes are electromagnetic modes with atypical  $\phi$  profiles. Also, both modes propagate in the ion diamagnetic direction. MT modes usually propagate in the electron diamagnetic direction opposite to what is calculated for the tearing-parity modes. To further identify these modes, scans over the ion temperature, the electron temperature and density gradient scale lengths, and the electron  $\beta$  are shown in Figure 5. While MT modes are expected to be stabilized at high  $a/L_n$ , the tearing-like mode at  $k_\theta \rho_s = 0.3$  is found to be driven by mainly  $a/L_n$  above a critical  $\beta \sim 0.008$ , with a change in the real frequency sign at  $a/L_n$  below experimental values. In addition, this

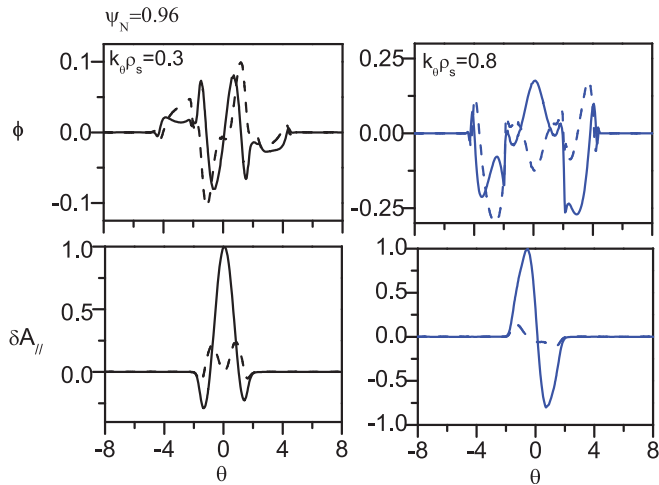


FIG. 4. Normalized field eigenfunctions at  $\psi_N = 0.96$  (non-lithiated discharge) plotted as a function of the poloidal angle  $\theta$  for  $k_{\theta}\rho_s$  specified in the legend.

tearing-like mode shows low sensitivity to  $a/L_{T_e}$ , as may be seen in Figure 5(b). However,  $a/L_n$  and  $\beta$  scans exhibit branches labeled in green in Figures 5(c) and 5(d). The analysis of each branch eigenfunction parity shows both ballooning-like structures (B) and tearing-like parities (T) around the experimental values. A scan over the electron

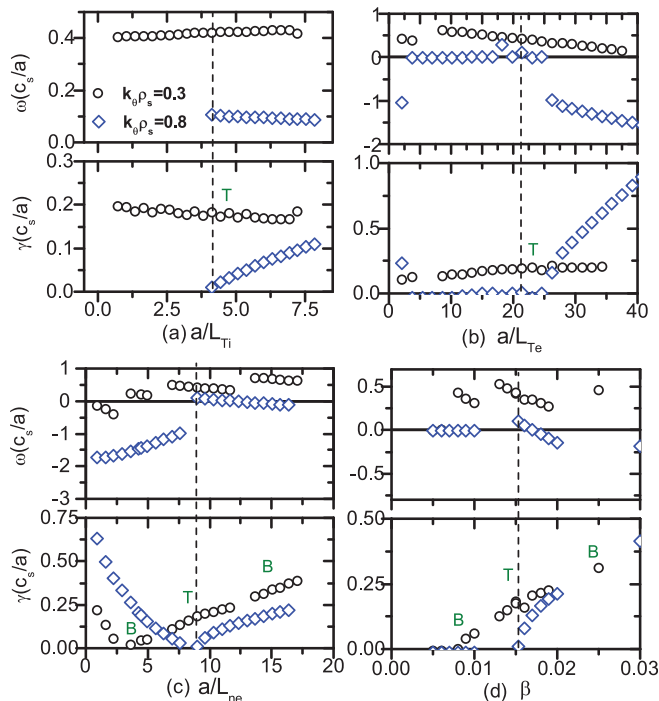


FIG. 5. Example of parameter scans (non-lithiated discharge) performed at  $\Psi_N = 0.96$  and  $k_{\theta}\rho_s$  specified in the legend. (a) Parameter scan performed over the ion temperature gradient scale length. (b) Parameter scan performed over the electron temperature gradient scale length. (c) Parameter scan performed over the density gradient scale length. (d) Parameter scan performed over the electron  $\beta$ . The x-axis in (c) is the  $(a/L_{ne})$  electron density gradient scale length; however in the parameter scans over  $a/L_n$ , all the species  $a/L_{ns}$  are scaled by the same factor to maintain charge neutrality (when the Debye shielding parameter is not enabled). Dashed vertical lines are the experimentally inferred values.

collision frequency (not shown) shows a decrease in the growth rate as the collision rate is increased. Several distinct branches appear in this scan, all having tearing-like parities. The parameter scans made at a wavenumber  $k_{\theta}\rho_s = 0.8$  show a clear dependence of this ballooning-like mode on  $\beta$ . In addition, this KBM (kinetic ballooning mode)-like mode is found to be driven by  $a/L_{n,T}$  above a critical  $\beta$ , with  $a/L_{n,T}$  and  $\beta$  critical values found near experimental values.

Tearing-parity modes propagating in the ion drift direction are found unstable at the mid-pedestal of the *lithiated discharge* ( $\Psi_N = 0.90$ ). Here also, parameter scans performed at  $k_{\theta}\rho_s = 0.1$  and  $0.3$  show that both tearing-parity modes are mainly driven by  $a/L_n$  above critical values. Ballooning-like eigenmodes are found unstable at higher wavenumbers. For instance, the mode at  $k_{\theta}\rho_s = 0.8$ , propagating in the ion drift direction, presents a ballooning-like structure. The parameter scans confirm that this mode is driven by  $a/L_n$  and  $a/L_T$  above a critical  $\beta$ , a sign of KBM-like modes. A few modes unstable at  $k_{\theta}\rho_s \leq 0.1$  and electrostatic modes unstable for  $\sim 1 \leq k_{\theta}\rho_s \leq \sim 10$  are observed at mid-pedestal of both discharges. Some of these electrostatic modes present atypical eigenfunction structures peaking off  $\theta = 0$ . The modes are not understood and will be discussed in a future publication.

Moving towards the separatrix at  $\Psi_N = 0.99$ , the *non-lithiated discharge* wavenumber scan shown in Figure 2(b) highlights two maxima in the growth rate profile, with the growth rate peaking at  $k_{\theta}\rho_s \sim 0.3$  for the first group and at  $k_{\theta}\rho_s \sim 0.8$  for the second group. These electrostatic modes peak away from the outboard midplane, as may be seen in Figure 6. Both modes are mainly driven by  $(a/L_{T_e})$  above critical values, suggesting the presence of TE modes.

Electrostatic modes are also found unstable for the *lithiated discharge*, with  $\phi$  peaking away from the outboard

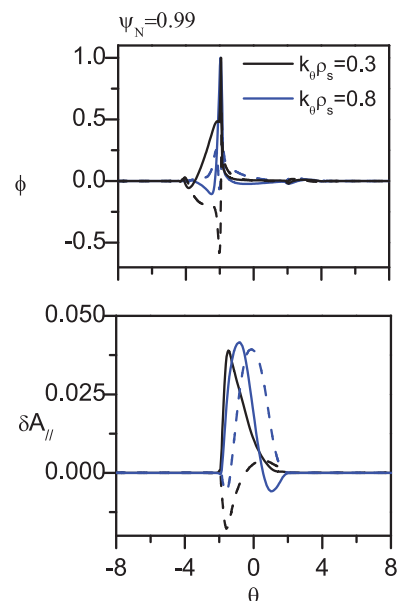


FIG. 6. Normalized field eigenfunctions at  $\psi_N = 0.99$  (non-lithiated discharge) plotted as a function of the poloidal angle  $\theta$  for  $k_{\theta}\rho_s$  specified in the legend.

midplane. For instance, the parameter scans performed at  $k_{\theta}\rho_s = 0.8$  show that this electrostatic mode is driven by  $a/L_{T_e}$  above a critical value, suggesting the presence of a TE mode. A few electromagnetic modes (modes with positive real frequencies in Figure 2(e)) are found unstable. The modes present a tearing-like parity at  $k_{\theta}\rho_s = 0.1$  and a ballooning-like parity at  $k_{\theta}\rho_s = 0.2$ . However, microtearing modes, or, MTMs are usually found unstable at the pedestal top and towards the core at high  $\beta$  but low  $a/L_p$ . KBM-like modes are usually found unstable at steep pressure gradients. These electromagnetic modes are also not yet understood and will be discussed in a future publication.

## B. Electron-scale wavenumbers

Electrostatic modes (ETG) are found unstable across the pedestal region for the non-lithiated discharge. Unstable ETG modes with higher growth rates are predicted from mid-pedestal outwards for the lithiated discharge, with scales exceeding  $k_{\theta}\rho_s = 100$  for both discharges. The ETG modes are usually found unstable, when the temperature gradient exceeds a critical value. The ETG modes are stabilized by the density gradient, when  $\eta_e = (a/L_{T_e})/(a/L_{n_e})$  exceed a linear critical value<sup>38</sup> of  $\sim 1.2$ . Table IV shows the experimental and numerical  $\eta_e$  values at several flux surfaces within the pedestal. From mid pedestal outwards of both discharges, ETG modes are found unstable for an average  $\eta_{e,linear} \sim 1.5$ . The average experimental  $\eta_{e,exp}$  is equal to 2.2, close to the experimental  $\eta_e \sim 2$  found at the H-mode edge of the ASDEX Upgrade.

For instance, the parameter scans performed at  $k_{\theta}\rho_s = 60$  (mid-pedestal non-lithiated discharge) highlight that this electrostatic mode is driven by  $a/L_{T_e}$  above a critical value of  $\sim 15$ , as shown in Figure 7(a), and is stabilized with increasing  $a/L_n$ . This mode is also destabilized with increasing  $\beta$ . Figure 7(a) shows ETG growth rates as a function of  $a/L_{T_e}$  for several  $\Psi_N$  within the pedestal region. A clear change in the ETG stability between both discharges may be seen in the figure, with the lithiated critical  $a/L_{T_e}$  being reduced when compared to the non-lithiated critical  $a/L_{T_e}$  at a same flux surface, as observed at intermediate plasma shaping.<sup>16</sup> Here also, the decrease of the lithiated  $a/L_{n_e} \sim 10$  when compared to the non-lithiated  $a/L_{n_e} \sim 18.5$  may explain the reduction of the critical drive threshold, since ETG modes are expected to be linearly stabilized with increasing  $a/L_n$ . By interchanging  $a/L_{n_e}$  between both study cases at  $\Psi_N = 0.99$ , it can be seen in Figure 7(b) that the

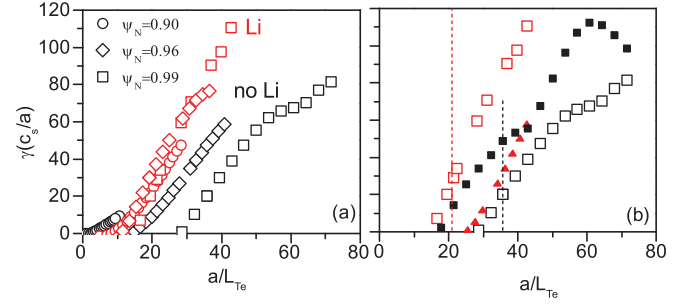


FIG. 7. (a) ETG growth rates as a function of  $a/L_{T_e}$  at  $\psi_N$  indicated in the legend and  $k_{\theta}\rho_s = 60$  (expect for the non-lithiated discharge at  $\psi_N = 0.90$  and  $k_{\theta}\rho_s = 30$ ). Black symbols represent the non-lithiated discharge, red symbols represent the lithiated discharge. (b) ETG growth rates as a function of  $a/L_{T_e}$  at  $\psi_N = 0.99$ . The filled symbols represent scans performed with interchanged  $a/L_{n_e}$ . Squares represent the non-lithiated plasma parameters with the lithiated  $a/L_{n_e}$ . Triangles represent the lithiated plasma parameters with the non-lithiated  $a/L_{n_e}$ . The dashed vertical lines are the experimental values of  $a/L_{T_e}$ .

ETG threshold is reduced with reduced electron density gradient taken from the lithiated discharge, keeping the other non-lithiated gradients fixed.

## IV. INITIAL COMPARISON BETWEEN INTERMEDIATE AND HIGH PLASMA SHAPING

In order to evaluate the effect of the shaping on edge instabilities, results for non-lithiated discharges at different shaping are compared since the lithium dose differs between lithiated discharges. The experimentally measured non-lithiated electron profiles are shown in Figure 8. Note that the steady neutral beam heating power for the discharge at intermediate shaping was 4 MW. As can be seen, close  $T_e$  trends are observed for  $\Psi_N > 0.95$ , with the highly shaped pedestal top extending further inwards. The electron density  $n_e$  is higher for the highly shaped discharge. The low- $k_{\theta}$  instabilities identified herein are also compared to the results published in Ref. 16, as summarized in Table V. Both studies highlight the presence of MT modes at the pedestal-top, with no sign of ITG in this study. KB modes are found unstable at mid-pedestal, competing with TE modes at intermediate shaping.<sup>16</sup> TE modes are found unstable near the separatrix in this work. No obvious difference can be firmly linked to the plasma shaping based on this comparison of

TABLE IV. ETG critical drive:  $\eta_{e,exp} = a/L_{T_e}/a/L_{n_e}$  is calculated using experimental gradient values.  $\eta_{e,linear} = a/L_{T_e,c}/a/L_{n_e}$  is calculated using the numerical critical temperature gradient values and the experimental density gradient values.

	No lithium		Lithium	
	$\eta_{e,exp}$	$\eta_{e,linear}$	$\eta_{e,exp}$	$\eta_{e,linear}$
$\Psi_N = 0.9$	10.7	5	2.6	1.4
$\Psi_N = 0.96$	2.4	1.6	2.4	1.4
$\Psi_N = 0.99$	1.9	1.5	2.2	1.6

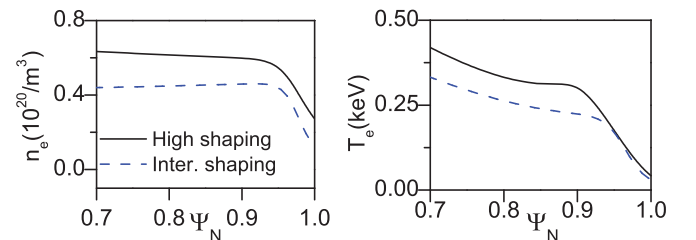


FIG. 8. Electron density ( $n_e$ ) and temperature ( $T_e$ ) experimentally inferred profiles as a function of  $\psi_N$ . The highly shaped non-lithiated discharge is represented in black lines. The non-lithiated discharge at intermediate shaping (labeled inter. shaping) is represented in blue dashed lines.

TABLE V. Comparison of linear low- $k_\theta$  instabilities between non-lithiated discharges recorded at intermediate and high shaping.

	High shaping ( $\delta \sim 0.6 - 0.7 - \kappa \sim 2.2$ )	Intermediate shaping ( $\delta \sim 0.46 - \kappa \sim 1.8$ )
$\Psi_N = 0.9$	MTM	ITG $\rightarrow$ MTM
$\Psi_N = 0.96$	Tearing-parity $\rightarrow$ KBM	TEM/KBM
$\Psi_N = 0.99$	TEM	

microinstabilities. To further assess the effect of the plasma shaping, additional calculations are carried out at mid-pedestal ( $\Psi_N = 0.96$ ) of non-lithiated discharges. The calculations are performed using the plasma parameters inferred for the discharge at intermediate shaping with the equilibrium parameters inferred for the discharge at high shaping and vice versa. Figure 9 presents the growth rates obtained with interchanged equilibria and gradients. Since some gradients differ for both discharges (see the Appendix), the “consistent” simulations are also presented in this figure. At long wavelengths shown in Figures 9(a) and 9(c), the growth rate spectra are altered by both equilibria and gradients. Electrostatic modes are unstable at intermediate plasma parameters, while electromagnetic modes are found unstable at highly shaped plasma parameters, with any equilibrium. The equilibrium shaping mainly affects the electrostatic modes stability. These modes are found more unstable at high plasma shaping. The eigenfunction structures for these modes are also altered when interchanging equilibria. No major change is observed by interchanging equilibria when using the highly shaped plasma parameters. The eigenfunction structures and parities are conserved. On the electron-scale wavenumbers, ETG modes are found more unstable when using the highly shaped equilibrium parameters with any plasma profiles. A future work will be to perform the parameter scans around experimentally inferred  $\delta$  and/or  $\kappa$  to evaluate the effect of the shaping on edge stability.

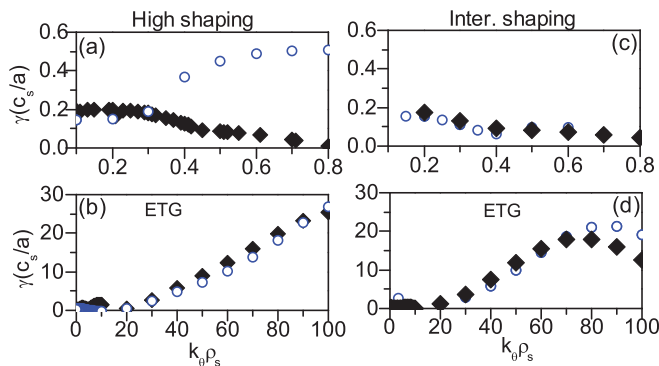


FIG. 9. Wavenumber scans performed at  $\Psi_N = 0.96$  for non-lithiated discharges. (a) and (b) Low- $k$  and high- $k$  growth rates calculated using the non-lithiated, highly shaped plasma equilibrium (shot #132543). (c) and (d) Low- $k$  and high- $k$  growth rates calculated using the non-lithiated plasma equilibrium at intermediate shaping (shot #129015). In all figures, black squares are calculated using the plasma parameters at high shaping. Blue circles are calculated using the plasma parameters at intermediate shaping.

## V. DISCUSSION AND SUMMARY

This linear gyrokinetic study characterizes the effect of high lithium doses in highly shaped discharges on edge microinstabilities. It is experimentally observed that ELMs are suppressed at high lithium doses. Also observed in lithiated discharges are a reduction of the  $D_\alpha$  emission and an improved energy confinement. The experimental profiles are also altered. A widening of the pedestal region in lithiated discharges is clearly observed from the density profiles. The temperature profiles follow close trends for both discharges for  $\Psi_N > 0.90$ , with a clear increase of the lithiated temperature profiles when moving towards the core.

Spectra of the eigenvalues, calculated at flux surfaces moving from the pedestal top towards the separatrix for both discharges, show series of competing eigenmodes propagating in both the ion and electron drift directions for ion-scale wavenumbers. At higher wavenumbers, the spectra show modes mainly propagating in the electron drift direction.

MT modes dominate the pedestal-top mainly without lithium. Tearing-parity and KB modes are found unstable at mid-pedestal, and TE modes are linearly unstable near the separatrix for both discharges. At short wavelengths, ETG modes are found unstable mainly from mid-pedestal outwards for an average  $\eta_{e,exp} \sim 2.2$ . As a consequence of reduced density gradients, the  $a/L_T$  threshold for ETG modes is reduced in the presence of lithium, when compared to the non-lithiated discharge.

Since MTMs are stabilized at the lithiated pedestal-top, electron heat transport is then reduced allowing the temperature and pressure to increase inwards. The reduced lithiated edge pressure gradient and current density lead to the reduction or elimination of edge localized modes, as observed experimentally. The reduction of the lithiated ETG threshold may explain the near separatrix electron temperature profile stiffness between both discharges observed experimentally. To quantify heat and particle fluxes, nonlinear local calculations have been initiated.

The preliminary study of the effect of the plasma shaping on edge microinstabilities shows that the low- $k$  electrostatic modes at intermediate plasma profiles are more unstable with higher shaping. Electrostatic ETG modes at the highest  $k_\theta \rho_s$  are also found more unstable at high shaping with any plasma profiles. As already mentioned, some eigenfunction structures mainly associated with low to intermediate- $k_\theta$  electrostatic eigenmodes show atypical  $\phi$  structures. These atypical  $\phi$  profiles are often maximum off the outboard midplane. The analysis of these modes is left for future work. Global gyrokinetic edge simulations are also left for future work.

## ACKNOWLEDGMENTS

We thank Eliot Feibush and Irena Johnson (systems and networking division) for assistance with PPPL clusters. This work was supported by the U.S. Department of Energy under Contract No. DE-AC02-09CH11466. The digital data for this paper can be found at <http://arks.princeton.edu/ark:/88435/dsp01n870zt23w>.

## APPENDIX: PLASMA EQUILIBRIUM PARAMETERS

TABLE VI. Normalized plasma equilibrium parameters at  $\Psi_N = 0.96$ . Shot #129015 is a non-lithiated discharge recorded at intermediate plasma shaping. Shots #132543 and #132588 are non-lithiated and lithiated discharges recorded at high plasma shaping.  $q_{95}$  represents the edge safety factor,  $\beta'$  characterizes the pressure gradient,  $\hat{s}$  represents the magnetic shear, and  $Z_{eff}$  is the effective charge.

Shot	$q_{95}$	$\beta'$	$\hat{s}$	$Z_{eff}$	$\beta$	$a/L_{T_e}$	$a/L_{T_i}$	$a/L_{T_e}$	$a/L_{n_e}$	$a/L_{n_i}$	$a/L_{n_e}$
#129015	9.15	-0.54	7.11	1.98	0.01	25.9	2.94	2.94	11.92	11.06	15.4
#132543	7.53	-0.62	7.5	2.56	0.015	21.5	4.2	4.2	9	4.7	110
#132588	8.59	-0.19	6.95	3.68	0.003	19.3	3.9	3.9	8.04	8.25	48

- <sup>1</sup>M. Ono, M. G. Bell, R. Kaita, H. W. Kugel, J.-W. Ahn, J. P. Allain, D. Battaglia, R. E. Bell, J. M. Canik, S. Ding, S. Gerhardt, T. K. Gray, W. Guttenfelder, J. Hosea, M. A. Jaworski, J. Kallman, S. Kaye, B. P. LeBlanc, R. Maingi, D. K. Mansfield, A. McLean, J. Menard, D. Muller, B. Nelson, R. Nygren, S. Paul, R. Raman, Y. Ren, P. Ryan, S. Sabbagh, F. Scotti, C. Skinner, V. Soukhanovskii, V. Surla, C. N. Taylor, J. Timberlake, H. Y. Yuh, and L. E. Zakharov, "Recent progress of NSTX lithium program and opportunities for magnetic fusion research," *Fusion Eng. Des.* **87**(10), 1770–1776 (2012).
- <sup>2</sup>J. W. Connor, "A review of models for ELMs," *Plasma Phys. Controlled Fusion* **40**(2), 191 (1998).
- <sup>3</sup>P. B. Snyder, H. R. Wilson, J. R. Ferron, L. L. Lao, A. W. Leonard, T. H. Osborne, A. D. Turnbull, D. Mossessian, M. Murakami, and X. Q. Xu, "Edge localized modes and the pedestal: A model based on coupled peeling-ballooning modes," *Phys. Plasmas* **9**(5), 2037–2043 (2002).
- <sup>4</sup>H. R. Wilson, P. B. Snyder, G. T. A. Huysmans, and R. L. Miller, "Numerical studies of edge localized instabilities in tokamaks," *Phys. Plasmas* **9**(4), 1277–1286 (2002).
- <sup>5</sup>A. Diallo, J. Canik, T. Gerler, S.-H. Ku, G. J. Kramer, T. Osborne, P. Snyder, D. R. Smith, W. Guttenfelder, R. E. Bell, D. P. Boyle, C.-S. Chang, B. P. LeBlanc, R. Maingi, M. Podest, and S. Sabbagh, "Progress in characterization of the pedestal stability and turbulence during the edge-localized-mode cycle on national spherical torus experiment," *Nucl. Fusion* **53**(9), 093026 (2013).
- <sup>6</sup>A. Diallo, J. W. Hughes, M. Greenwald, B. LaBombard, E. Davis, S.-G. Baek, C. Theiler, P. Snyder, J. Canik, J. Walk, T. Golfopoulos, J. Terry, M. Churchill, A. Hubbard, M. Porkolab, L. Delgado-Aparicio, M. L. Reinke, A. White, and Alcator C-Mod Team, "Observation of edge instability limiting the pedestal growth in tokamak plasmas," *Phys. Rev. Lett.* **112**, 115001 (2014).
- <sup>7</sup>I. Holod, D. Fulton, and Z. Lin, "Microturbulence in DIII-D tokamak pedestal. II. Electromagnetic instabilities," *Nucl. Fusion* **55**(9), 093020 (2015).
- <sup>8</sup>D. R. Hatch, D. Told, F. Jenko, H. Doerk, M. G. Dunne, E. Wolftrum, E. Viezzer, ASDEX Upgrade Team, and M. J. Pueschel, "Gyrokinetic study of ASDEX upgrade inter-elm pedestal profile evolution," *Nucl. Fusion* **55**(6), 063028 (2015).
- <sup>9</sup>R. A. Pitts, J. P. Coad, D. P. Coster, G. Federici, W. Fundamenski, J. Horacek, K. Krieger, A. Kukushkin, J. Likonen, G. F. Matthews, M. Rubel, J. D. Strachan, and JET-EFDA Contributors, "Material erosion and migration in tokamaks," *Plasma Phys. Controlled Fusion* **47**(12B), B303 (2005).
- <sup>10</sup>R. Maingi, D. P. Boyle, J. M. Canik, S. M. Kaye, C. H. Skinner, J. P. Allain, M. G. Bell, R. E. Bell, S. P. Gerhardt, T. K. Gray, M. A. Jaworski, R. Kaita, H. W. Kugel, B. P. LeBlanc, J. Manickam, D. K. Mansfield, J. E. Menard, T. H. Osborne, R. Raman, A. L. Roquemore, S. A. Sabbagh, P. B. Snyder, and V. A. Soukhanovskii, "The effect of progressively increasing lithium coatings on plasma discharge characteristics, transport, edge profiles and ELM stability in the national spherical torus experiment," *Nucl. Fusion* **52**(8), 083001 (2012).
- <sup>11</sup>R. Maingi, T. H. Osborne, M. G. Bell, R. E. Bell, D. P. Boyle, J. M. Canik, A. Diallo, R. Kaita, S. M. Kaye, H. W. Kugel, B. P. LeBlanc, S. A. Sabbagh, C. H. Skinner, and V. A. Soukhanovskii, "Dependence of recycling and edge profiles on lithium evaporation in high triangularity, high performance NSTX h-mode discharges," *J. Nucl. Mater.* **463**, 1134–1137 (2015).
- <sup>12</sup>R. Maingi, T. H. Osborne, B. P. LeBlanc, R. E. Bell, J. Manickam, P. B. Snyder, J. E. Menard, D. K. Mansfield, H. W. Kugel, R. Kaita, S. P. Gerhardt, S. A. Sabbagh, and F. A. Kelly, "Edge-localized-mode suppression through density-profile modification with lithium-wall coatings in the national spherical torus experiment," *Phys. Rev. Lett.* **103**, 075001 (2009).
- <sup>13</sup>D. P. Boyle, R. Maingi, P. B. Snyder, J. Manickam, T. H. Osborne, R. E. Bell, B. P. LeBlanc, and NSTX Team, "The relationships between edge localized modes suppression, pedestal profiles and lithium wall coatings in NSTX," *Plasma Phys. Controlled Fusion* **53**(10), 105011 (2011).
- <sup>14</sup>D. A. Gates, R. Maingi, J. Menard, S. Kaye, S. A. Sabbagh, G. Taylor, J. R. Wilson, M. G. Bell, R. E. Bell, S. Bernabei, J. Bialek, T. Biewer, W. Blanchard, J. Boedo, C. Bush, M. D. Carter, W. Choe, N. Crocker, D. S. Darrow, W. Davis, L. Delgado-Aparicio, S. Diem, J. Ferron, A. Field, J. Foley, E. D. Fredrickson, R. Harvey, R. E. Hatcher, W. Heidbrink, K. Hill, J. C. Hosea, T. R. Jarboe, D. W. Johnson, R. Kaita, C. Kessel, S. Kubota, H. W. Kugel, J. Lawson, B. P. LeBlanc, K. C. Lee, F. Levinton, J. Manickam, R. Maqueda, R. Marsala, D. Mastrovito, T. K. Mau, S. S. Medley, H. Meyer, D. R. Mikkelsen, D. Mueller, T. Munsat, B. A. Nelson, C. Neumeyer, N. Nishino, M. Ono, H. Park, W. Park, S. Paul, W. Peebles, M. Peng, C. Phillips, A. Pigarov, R. Pinsky, A. Ram, S. Ramakrishnan, R. Raman, D. Rasmussen, M. Redi, M. Rensink, G. Rewoldt, J. Robinson, P. Roney, L. Roquemore, E. Ruskov, P. Ryan, H. Schneider, C. H. Skinner, D. R. Smith, A. Sontag, V. Soukhanovskii, T. Stevenson, D. Stotler, B. Stratton, D. Stutman, D. Swain, E. Synakowski, Y. Takase, K. Tritz, A. von Halle, M. Wade, R. White, J. Wilgen, M. Williams, W. Zhu, S. J. Zweben, R. Akers, P. Beiersdorfer, R. Betti, and T. Bigelow, "Effect of plasma shaping on performance in the national spherical torus experiment," *Phys. Plasmas* **13**(5), 056122 (2006).
- <sup>15</sup>E. A. Belli, G. W. Hammett, and W. Dorland, "Effects of plasma shaping on nonlinear gyrokinetic turbulence," *Phys. Plasmas* **15**(9), 092303 (2008).
- <sup>16</sup>J. M. Canik, W. Guttenfelder, R. Maingi, T. H. Osborne, S. Kubota, Y. Ren, R. E. Bell, H. W. Kugel, B. P. LeBlanc, and V. A. Soukhanovskii, "Edge microstability of NSTX plasmas without and with lithium-coated plasma-facing components," *Nucl. Fusion* **53**(11), 113016 (2013).
- <sup>17</sup>R. D. Hazeltine, D. Dobrott, and T. S. Wang, "Kinetic theory of tearing instability," *Phys. Fluids* **18**(12), 1778–1786 (1975).
- <sup>18</sup>W. Guttenfelder, J. Candy, S. M. Kaye, W. M. Nevins, R. E. Bell, G. W. Hammett, B. P. LeBlanc, and H. Yuh, "Scaling of linear microtearing stability for a high collisionality national spherical torus experiment discharge," *Phys. Plasmas* **19**(2), 022506 (2012).
- <sup>19</sup>B. B. Kadomtsev and O. P. Pogutse, "Trapped particles in toroidal magnetic systems," *Nucl. Fusion* **11**(1), 67 (1971).
- <sup>20</sup>R. R. Dominguez and R. E. Waltz, "Tokamak transport code simulations with drift wave models," *Nucl. Fusion* **27**(1), 65 (1987).
- <sup>21</sup>G. Rewoldt, Z. Lin, and Y. Idomura, "Linear comparison of gyrokinetic codes with trapped electrons," *Comput. Phys. Commun.* **177**(10), 775–780 (2007).
- <sup>22</sup>Y. C. Lee, J. Q. Dong, P. N. Guzdar, and C. S. Liu, "Collisionless electron temperature gradient instability," *Phys. Fluids* **30**(5), 1331 (1987).
- <sup>23</sup>E. A. Frieman, G. Rewoldt, W. M. Tang, and A. H. Glasser, "General theory of kinetic ballooning modes," *Phys. Fluids* **23**(9), 1750–1769 (1980).
- <sup>24</sup>E. A. Belli and J. Candy, "Fully electromagnetic gyrokinetic eigenmode analysis of high-beta shaped plasmas," *Phys. Plasmas* **17**(11), 112314 (2010).
- <sup>25</sup>W. Guttenfelder, J. L. Peterson, J. Candy, S. M. Kaye, Y. Ren, R. E. Bell, G. W. Hammett, B. P. LeBlanc, D. R. Mikkelsen, W. M. Nevins, and H. Yuh, "Progress in simulating turbulent electron thermal transport in NSTX," *Nucl. Fusion* **53**(9), 093022 (2013).

- <sup>26</sup>W. Dorland, F. Jenko, M. Kotschenreuther, and B. N. Rogers, "Electron temperature gradient turbulence," *Phys. Rev. Lett.* **85**, 5579–5582 (2000).
- <sup>27</sup>D. Dickinson, C. M. Roach, S. Saarelma, R. Scannell, A. Kirk, and H. R. Wilson, "Kinetic instabilities that limit  $\beta$  in the edge of a tokamak plasma: A picture of an  $h$ -mode pedestal," *Phys. Rev. Lett.* **108**, 135002 (2012).
- <sup>28</sup>F. Jenko, W. Dorland, M. Kotschenreuther, and B. N. Rogers, "Electron temperature gradient driven turbulence," *Phys. Plasmas* **7**(5), 1904–1910 (2000).
- <sup>29</sup>F. Jenko, W. Dorland, and G. W. Hammett, "Critical gradient formula for toroidal electron temperature gradient modes," *Phys. Plasmas* **8**(9), 4096–4104 (2001).
- <sup>30</sup>F. Jenko and A. Kendl, "Stellarator turbulence at electron gyroradius scales," *New J. Phys.* **4**(1), 35 (2002).
- <sup>31</sup>E. Wang, X. Xu, J. Candy, R. J. Groebner, P. B. Snyder, Y. Chen, S. E. Parker, W. Wan, G. Lu, and J. Q. Dong, "Linear gyrokinetic analysis of a DIII-D  $h$ -mode pedestal near the ideal ballooning threshold," *Nucl. Fusion* **52**(10), 103015 (2012).
- <sup>32</sup>D. P. Fulton, Z. Lin, I. Holod, and Y. Xiao, "Microturbulence in DIII-D tokamak pedestal. I. Electrostatic instabilities," *Phys. Plasmas* **21**(4), 042110 (2014).
- <sup>33</sup>B. F. McMillan, X. Lapillonne, S. Brunner, L. Villard, S. Jolliet, A. Bottino, T. Görler, and F. Jenko, "System size effects on gyrokinetic turbulence," *Phys. Rev. Lett.* **105**, 155001 (2010).
- <sup>34</sup>A. Cooper, "Variational formulation of the linear MHD stability of 3d plasmas with noninteracting hot electrons," *Plasma Phys. Controlled Fusion* **34**(6), 1011 (1992).
- <sup>35</sup>J. A. Baumgaertel, E. A. Belli, W. Dorland, W. Guttenfelder, G. W. Hammett, D. R. Mikkelsen, G. Rewoldt, W. M. Tang, and P. Xanthopoulos, "Simulating gyrokinetic microinstabilities in stellarator geometry with GS2," *Phys. Plasmas* **18**(12), 122301 (2011).
- <sup>36</sup>A. M. Dimits, G. Bateman, M. A. Beer, B. I. Cohen, W. Dorland, G. W. Hammett, C. Kim, J. E. Kinsey, M. Kotschenreuther, A. H. Kritz, L. L. Lao, J. Mandrekas, W. M. Nevins, S. E. Parker, A. J. Redd, D. E. Shumaker, R. Sydora, and J. Weiland, "Comparisons and physics basis of tokamak transport models and turbulence simulations," *Phys. Plasmas* **7**(3), 969–983 (2000).
- <sup>37</sup>P. W. Terry, D. Carmody, H. Doerk, W. Guttenfelder, D. R. Hatch, C. C. Hegna, A. Ishizawa, F. Jenko, W. M. Nevins, I. Predebon, M. J. Pueschel, J. S. Sarff, and G. G. Whelan, "Overview of gyrokinetic studies of finite-microturbulence," *Nucl. Fusion* **55**(10), 104011 (2015).
- <sup>38</sup>F. Jenko, D. Told, P. Xanthopoulos, F. Merz, and L. D. Horton, "Gyrokinetic turbulence under near-separatrix or nonaxisymmetric conditions," *Phys. Plasmas* **16**(5), 055901 (2009).